Full length article

Joint investigation of strain partitioning and chemical partitioning in ferrite-containing TRIP-assisted steels

Xiaodong Tan[a,*], Dirk Ponge[b,*], Wenjun Lu[b,*], Yunbo Xu[c], Huansheng He[a], Jun Yan[a], Di Wu[c], Dierk Raabe[b]

[a] *School of Materials and Energy, Southwest University, Tiansheng-Road 2, Beibei District, Chongqing 400715, PR China*
[b] *Max-Planck-Institut für Eisenforschung GmbH, Max-Planck-Str. 1, Düsseldorf 40237, Germany*
[c] *State Key Laboratory of Rolling and Automation, Northeastern University, Shenyang 110819, PR China*

ABSTRACT

We applied two types of hot-rolling direct quenching and partitioning (HDQ&P) schemes to a low-C low-Si Al-added steel and obtained two ferrite-containing TRIP-assisted steels with different hard matrix structures, viz, martensite or bainite. Using quasi in-situ tensile tests combined with high-resolution electron back-scattered diffraction (EBSD) and microscopic digital image correlation (μ-DIC) analysis, we quantitatively investigated the TRIP effect and strain partitioning in the two steels and explored the influence of the strain partitioning between the soft and hard matrix structures on the TRIP effect. We also performed an atomic-scale analysis of the carbon partitioning among the different phases using atom probe tomography (APT). The results show that the strain mainly localizes in the ferrite in both types of materials. For the steel with a martensitic hard-matrix, a strong strain contrast exists between ferrite and martensite, with the local strain difference reaching up to about 75% at a global strain of 12.5%. Strain localization bands initiated in the ferrite rarely cross the ferrite/martensite interfaces. The low local strain (2%–10%) in the martensite regions leads to a slight TRIP effect with a transformation ratio of the retained austenite of about 7.5%. However, for the steel with bainitic matrix, the ferrite and bainite undergo more homogeneous strain partitioning, with an average local strain in ferrite and bainite of 15% and 8%, respectively, at a global strain of 12.5%. The strain localization bands originating in the ferrite can cross the ferrite/bainite (F/B) interfaces and increase the local strain in the bainite regions, resulting in an efficient TRIP effect. In that case the transformation ratio of the retained austenite is about 41%. The lower hardness difference between the ferrite and bainite of about 178 HV, compared with that between the ferrite and martensite of about 256 HV, leads to a lower strain contrast at the ferrite/bainite interfaces, thus retarding interfacial fracture. Further microstructure design for TRIP effect optimization should particularly focus on adjusting the strength contrast among the matrix structures and tuning strain partitioning to enhance the local strain partitioning into the retained austenite.

1. Introduction

Driven by the increasing demands for safe and lightweight automotive materials, significant research efforts have been devoted to the development of advanced high strength steels (AHSS) with good combination of strength and ductility [1–3]. Ductility enhancement through the martensitic transformation of retained austenite, the so-called transformation induced plasticity (TRIP) effect, triggered the design of TRIP-assisted multiphase steels, such as conventional TRIP steel, quenched and partitioned (Q&P) steel and medium manganese steel [4–9].

Numerous studies show that the premise for an effective TRIP behavior is a high volume fraction of retained austenite that transforms during deformation [10–13]. However, incomplete transformation of the retained austenite is a prevalent problem for TRIP-assisted steels, especially for those with a matrix structure consisting of soft and hard microstructure regions [14–17]. The mechanical stability of the retained austenite is a crucial factor controlling the transformation ratio [18,19]. A number of studies have revealed the important effects of the chemical composition [20], size [12], morphology [21], distribution [22] and crystal orientation [23] of the retained austenite on its mechanical stability, while no systematic quantitative research illuminated the specific relation between the strain distribution in the matrix, the strain partitioning among the different microstructure components and the mechanical stability of the retained austenite [24–26]. For TRIP-assisted multiphase steels,

* Corresponding authors.
 E-mail addresses: tanxd2017@swu.edu.cn (X. Tan), d.ponge@mpie.de (D. Ponge), w.lu@mpie.de (W. Lu).

the strength difference among adjacent phases results in strain partitioning and as a consequence in an inhomogeneous strain and stress distribution during deformation [27,28]. Since the retained austenite, depending on its composition and stability, requires a certain loading condition to undergo martensitic transformation, the strain partitioning among the microstructure components has a crucial influence on the TRIP effect [29,30]. Also, strain localization and interfacial damage initiation in such multiphase microstructures depend on such load partitioning effects [31−33]. These findings underline the necessity to conduct studies where strain partitioning, the TRIP effect and damage initiation in TRIP-assisted multiphase steels are jointly considered [34]. A quantitative study of these key features requires in-situ (or quasi in-situ) tensile testing in conjunction with high resolution electron back-scattered diffraction (EBSD) and microscopic digital image correlation (μ-DIC) strain mapping [20,35,36]. By combining μ-DIC with EBSD probing, we investigated the strain partitioning and the TRIP effect in a ferrite-containing Q&P steel [20]. We found that a strong strain contrast exists between the ferrite and martensite. The ferrite/martensite (F/M) fraction ratio and martensite morphology have crucial influences on the strain partitioning and the TRIP effect. Our previous work also revealed that the transformation ratio of retained austenite in the TRIP steel with a matrix consisting of ferrite, bainite and martensite is much larger than that in the TRIP steel with a matrix composed of only ferrite and martensite [16]. It was inferred that this phenomenon may result from the strain partitioning between the soft and hard matrix structures. The introduction of bainite in a ferrite-containing Q&P steel could improve the deformation uniformity among the matrix structures, thus enhancing the TRIP effect. However, to understand, prove and apply these effects, quantitative results about the strain partitioning and deformation-driven transformation effects in TRIP steels with different matrix structures are required, together with an improved probing and understanding of the role of the atomic-scale chemical partitioning across the hetero-interfaces.

Additionally, understanding of the origin of the mechanical partitioning among the main microstructural components requires to also map the chemical partitioning between them. This applies particularly for the strongest austenite stabilizer, viz. carbon, which has also the highest influence on the hardness of the different microstructure components [37]. For this reason it is important to map the carbon partitioning at near atomic-scale across the different microstructure regions in the TRIP-assisted multiphase steel [38,39].

In this work, we present results from quasi in-situ tensile tests in conjunction with high resolution EBSD and μ-DIC mapping conducted on two types of ferrite-containing TRIP-assisted steels, namely, one with martensitic and one with bainitic matrix. This procedure enables a quantitative investigation of strain partitioning and the TRIP effect. Combination of the strain maps and EBSD results allows us to identify correlations between size, orientation, structure, load partitioning, TRIP response and interfacial fracture, revealing the significance of strain partitioning on optimal utilization of the TRIP effect. The microstructure and micromechanical probing is combined with chemical probing: since X-ray diffraction (XRD) and energy dispersive spectrum analysis (EDS) cannot reveal differences in carbon concentration across these hetero-interfaces at near atomic-scale [40,41]. We study chemical partitioning here by atom probe tomography (APT) [42−45]. Based on these investigations, we develop a microstructure design strategy to optimize the TRIP effect for yielding a good compromise between strength, damage tolerance and ductility of ferrite-containing TRIP-assisted steels.

2. Experimental details

A low-C, low-Si, Al-added steel with chemical composition of Fe-0.18C-0.53Si-1.95Mn-1.46Al-0.08P (wt.%) was melted in a vacuum induction furnace and cast into a 150 kg ingot. Subsequently, the ingot was forged into slabs with a cross section of 60×60 mm. The transformation temperatures of the undeformed samples were measured using a Formastor-FII (FTF-340) dilatometer. The corresponding results are A_{c1}=712 °C, A_{c3}=1037 °C, A_{r1}=634 °C, A_{r3}=914 °C, M_s =421 °C and M_f =172 °C, respectively [16,20]. The heating rate and cooling rate for probing the A_{c1}, A_{c3}, A_{r1}, and A_{r3} temperatures were 0.05 °C/s. The critical quenching rate for a completely martensitic transformation of the steel is about −40 °C/s.

The A_{r1} and A_{r3} temperatures of both, the undeformed sample and the deformed sample (with compression strains at 1100 °C and 950 °C, respectively, of 30% and 20%) were measured on a DIL805 A/D dilatometer. The cooling rate for probing the A_{r1} and A_{r3} temperatures was −2 °C/s. The results for the undeformed sample are A_{r1}=638 °C and A_{r3}=884 °C, while those for the deformed sample are A_{r1}=659 °C and A_{r3}=907 °C. In addition, the M_s temperature of the deformed sample is 416 °C. This shows that the deformation results in an increase of the A_{r1} and A_{r3} temperatures.

We performed two different hot-rolling, direct quenching and partitioning (HDQ&P) processes, aiming at two different types of microstructures. Slab M was first austenized at 1200 °C for 2 h and then hot-rolled to 4 mm through 7 passes with a finish rolling temperature of about 910 °C. After air-cooling to about 760 °C, the sheet was directly quenched to about 370 °C with a cooling rate of about 190 °C/s and then heat treated for chemical partitioning at 350 °C for 5 min. Finally, it was air-cooled to room temperature [16]. The resulting material has a microstructure consisting of ferrite, martensite and retained austenite and will be hereafter referred to as sample M.

Following the same austenization process of slab M, slab B was first hot-rolled to 10 mm through 3 passes with the rolling temperature above 1000 °C and then air-cooled to about 950 °C. After hot rolling to 4 mm through 4 passes with a finish rolling temperature of about 800 °C, the sheet was air-cooled to 760 °C and then directly quenched to about 360 °C with a cooling rate of about 190 °C/s. Subsequently, it was heat treated for chemical partitioning in a furnace at 350 °C for 5 min, followed by air cooling to room temperature [16]. Since the A_{r1} and A_{r3} temperatures of the alloy are respectively 659 °C and 907 °C, sheet B was intercritically rolled during the hot rolling process. The resulting material has a microstructure consisting of ferrite, bainite, martensite and retained austenite and will be hereafter referred to as sample B. Deformation dilatometry results show that the M_s temperatures of the intercritical austenite in the samples M and B are, respectively, about 388 °C and 365 °C.

The mechanical properties were measured on a CMT5105-SANS machine. The volume fraction and average carbon concentration of the retained austenite were measured using a D/max2400 X-ray diffractometer (XRD) with Cu Kα radiation at room temperature. Details about the testing protocols and methods can be found elsewhere [16,46].

Secondary electron (SE) imaging and EBSD were performed to characterize the microstructures using a JEOL JSM-6500F SEM. The samples were mechanically ground and polished in diamond suspension followed by final polishing in colloidal silica suspension. For SE imaging, the samples were etched with 4% nital for 20 s. The EBSD measurements were carried out at 15 kV with the step size of 50 nm.

Atomic-scale carbon partitioning among the phases was investigated using APT. Samples for the APT measurements were prepared on a dual-beam focused ion beam (FIB) (FEI, Helios Nano-Lab 600i). APT characterization was conducted on a LEAP 3000X HR instrument (Cameca) in voltage mode at 75 K (−198 °C) [47,48]. The pulse fraction and the pulse rate were 15% and 200 kHz, respectively [38,49]. Reconstruction was carried out using the software Cameca IVAS ® [42,50]. Correlative APT/transmission electron microscopy (TEM) analysis was also carried out to characterize the carbon concentration in the retained austenite and bainite [47]. TEM analysis of the APT tips was performed on a Phillips CM20-TEM operated at 200 kV.

Quasi in-situ tensile tests in conjunction with EBSD and μ-DIC analyses were performed to investigate the TRIP effect and strain partitioning [20,31]. For the tensile tests, samples with 1.5 mm thickness, 2 mm width and 4 mm parallel length were prepared along the rolling direction. The samples were mechanically ground and polished, and then polished in colloidal silica suspension to relieve residual stresses [20]. For selecting local regions of interest for the μ-DIC analysis, a large field-of-view (60 × 80 μm) EBSD measurement was performed with the step size of 50 nm. A 20 min-plasma cleaning was carried out to remove the carbon contamination. To investigate the strain distribution evolution, a single layer of SiO_2 particles was homogeneously distributed on the polished sample surface. Different SEM detectors, such as SE and in-lens SE, were used to characterize the microstructure evolution. Using the ARAMIS software (GOM GmbH), we investigated the strain partitioning based on the in-lens SE images. To reveal the TRIP effect, an EBSD measurement was carried out again on the same local region after 3 (or 5) interrupted deformation steps, reaching a global strain in horizontal loading direction (ε_{avg}) of 12.5% (or 20.8%).

3. Results

3.1. Mechanical properties

The strength levels of the two samples are similar, with a yield strength and ultimate tensile strength (UTS) of about 540 MPa and 930 MPa, respectively. The total elongation and uniform elongation of sample B are 6%−8% larger than those of sample M. Sample B has a higher work hardening rate than sample M for a true strain regime above 4.4%, leading to its higher uniform elongation reaching up to about 16.5%. More detailed property results can be found in [16].

3.2. Microstructural characterization

Fig. 1 shows the SE images of the tested samples. Fig. 1(a) reveals that sample M consists of ferrite, martensite and retained austenite, with a ferrite fraction of about 47.9% ± 1.0% (in area fraction). With a ferrite fraction similar to that of sample M, 50.6% ± 1.4% (in area fraction), sample B is composed of ferrite, bainite, martensite and retained austenite, where the area fraction of martensite is about 9.6% ± 0.7%, as shown in Fig. 1(b). The ferrite fraction was measured based on 10−15 SE images of each sample. The reasons why bainite can be formed in sample B and the ferrite fractions are similar in the two samples had been discussed in our previous work [16]. The hardness of the ferrite and martensite in the sample M are, respectively, 197 ± 22 HV and 453 ± 62 HV. The hardness of the ferrite, bainite and martensite in sample B are 213 ± 16 HV, 391 ± 33 HV and 542 ± 41 HV, respectively. This means that the ferrite and martensite

in sample B have higher hardness than in sample M. The hardness difference between the ferrite and martensite in sample M is much larger than that between the ferrite and bainite in sample B.

Previously published XRD results showed that the volume fraction and average carbon concentration of the retained austenite in the undeformed sample M are 13.3 vol.% and 4.85 at.% [16]. The retained austenite in the undeformed sample B exhibits a larger fraction of 24.3 vol.% and a similar carbon content of 4.76 at.%. The transformation ratio of the retained austenite during the tensile deformation in the sample M is only 7.5%. Compared with sample M, specimen B exhibits a much higher fraction of TRIP regions, with the transformation ratio reaching up to 41.2%. The deformed samples were cut near the fracture zones of the tensile samples (within 10 mm). The local strains in the deformed samples were in the range of 15%−60%.

3.3. Atomic-scale analysis on carbon partitioning

The carbon partitioning between the martensite and retained austenite in sample M was investigated using APT, Fig. 2. Fig. 2(a) shows the carbon map of the martensite and retained austenite located in the local rectangular region shown in Fig. 2(b). The APT tip contains two retained austenite islands and one martensite lath with a thickness of about 260 nm. Fig. 2(c) shows the element distribution along the cylinder-1 passing through the retained austenite-1 and the martensite. The carbon distribution in the retained austenite-1 is inhomogeneous, with a carbon concentration of 4.0−6.5 at.%. The carbon concentration in the martensite is 0.5−1.5 at.%. Fig. 2(d) reveals the element distribution along the cylinder-2 crossing the retained austenite-2 and the martensite. With the value of 5.0−6.8 at.%, the carbon concentration of the retained austenite-2 is higher than that of the retained austenite-1.

Fig. 3 shows the APT results revealing the elemental partition among the different types of microstructure regions in sample B. Fig. 3(a) reveals the carbon map of the bainite and film-like retained austenite distributed in the local rectangular region shown in Fig. 3 (b). The thickness of the retained austenite film is about 25 nm. Fig. 3(c) shows the element distribution along the cylinder shown in Fig. 3(a). It can be seen that the carbon concentration in the retained austenite film is 4.8−6.5 at.%. The carbon is distributed inhomogeneously in the retained austenite film, with a concentration in the film center and at the B/RA interface of about 4.8 at.% and 6.5 at.%, respectively. The carbon concentration in the bainite is in the range of 0.2−0.8 at.%. Fig. 3(d) shows the carbon map of the bainite and blocky retained austenite located in the local rectangular region shown in Fig. 3(e). The element distribution along the cylinder crossing the bainite and blocky retained austenite is shown in Fig. 3(f). The carbon concentration in the retained austenite is 4.0−7.0 at.%. Compared with the retained austenite film shown in Fig. 3(a), the blocky
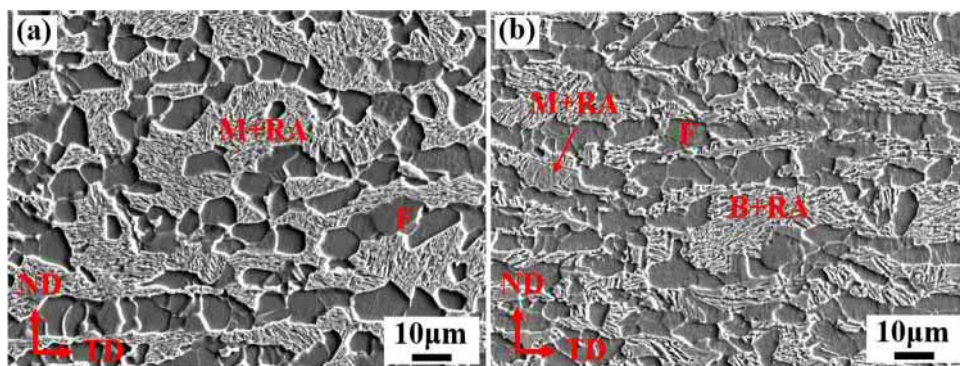

Fig. 1. SE images of the tested samples: (a) sample M (microstructure consisting of ferrite, martensite and retained austenite); (b) sample B (microstructure consisting of ferrite, bainite, martensite and retained austenite). "F", "B", "M", and "RA" represent ferrite, bainite, martensite and retained austenite, respectively.
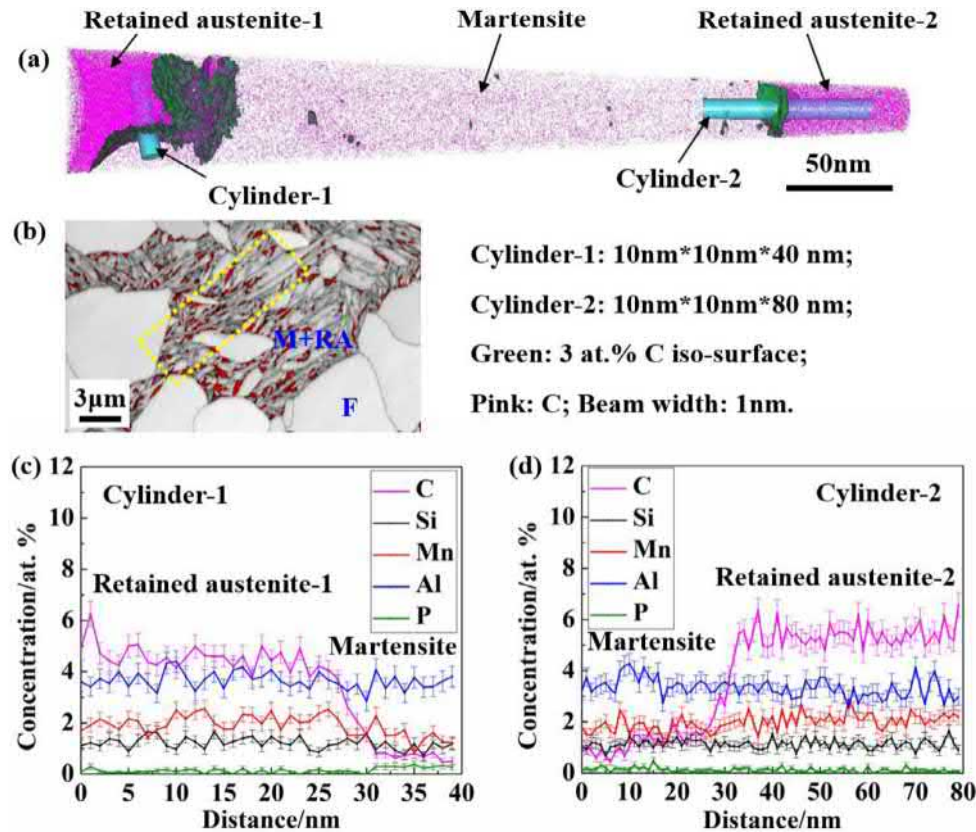
Fig. 2. APT results showing the element partition in the sample M (microstructure consisting of ferrite, martensite and retained austenite): (a) carbon map of the martensite and retained austenite; (b) EBSD image quality map (with retained austenite in red) showing the local region (yellow rectangle) chosen for site-specific preparation of the APT tip; (c) concentration profiles along the cylinder-1; (d) concentration profiles along the cylinder-2. All the concentrations are given in at.%. "F", "M", and "RA" represent ferrite, martensite and retained austenite, respectively. (For interpretation of the references to colour in this figure legend, the reader is referred to the web version of this article.)

retained austenite exhibits a stronger inhomogeneous carbon distribution, with the local enriched carbon concentration near the B/RA interface reaching up to 7.0 at.%. The carbon concentration in the bainite is 0.2−0.8 at.%. Fig. 3(g) shows the carbon map of the martensite distributed in the local rectangular region shown in Fig. 3(h). The element distribution along the cylinder is shown in Fig. 3(i). The carbon distribution in the martensite is almost homogenous and the carbon concentration is 1.5−3.0 at.%, which is 1.0−1.5 at.% higher than that of the martensite in sample M. Fig. 3(j) shows the carbon map of the ferrite, located in the local rectangular region shown in Fig. 3(k). The element distribution along the cylinder is shown in Fig. 3(l). With a concentration of 0.2−0.5 at.%, the carbon distribution is almost homogeneous inside the ferrite.

Further correlative TEM/APT analysis results for sample B are provided in Fig. 4. The EBSD map (Fig. 4(a)) shows the local region containing bainite laths and retained austenite films. APT samples were prepared in the region highlighted by the dashed yellow rectangle. Fig. 4(b) is the bright field image of the APT tip. Fig. 4(c) and (d) show the dark field image of the bainite and retained austenite, respectively. The carbon map of the bainite and retained austenite is revealed in Fig. 4(e) and (f). Fig. 4(g) shows the element distribution along the cylinder shown in Fig. 4(f). The carbon concentration in the retained austenite and bainite is 4.0−6.5 at.% and 0.5−1.2 at.%, respectively. The TEM results shown in Fig. 4(h) and (i) indicate a K-S orientation relationship between the bcc and fcc phases. The APT results shown in Figs. 2−4 reveal that no apparent partition of Si, Mn, Al and P exists among the ferrite, bainite, martensite and retained austenite, and the concentrations of these elements are respectively 1.0−2.0 at.%, 1.0−2.5 at.%, 3.0−4.5 at.% and 0.1−0.2 at.%. The formation of ferrite was achieved in 1−2 min during continuous cooling (air-cooling condition). Therefore, no partitioning of substitutional elements such as Si, Mn, Al and P was observed.

3.4. Quasi in-situ analysis on TRIP effect and strain partitioning

Fig. 5 shows the quasi in-situ EBSD results for material M. The image quality maps, Fig. 5(a1)−(a3), show that with increasing strain low index rate bands gradually appear in the local ferrite regions near the ferrite/martensite (F/M) interfaces and the narrow regions between two martensite islands, highlighted by the dashed yellow ellipses. The index rate in the local martensite region highlighted by the dashed yellow rectangle decreases with increasing global strain. The grain boundary maps shown in Fig. 5(b1)−(b3) reveal that the line fraction (fraction of the total length of specific GBs with respect to all GBs) of the subgrain structures with 2−5° misorientation increases with the increase of the global strain in the highlighted regions. These phenomena show that the strain is localized in the highlighted regions [26,32]. Fig. 5(c1)−(c3) show the IPF maps containing both the bcc and fcc phases. Orientation gradients enhance gradually in the ferrite grains with the increase of the average strain, while no significant orientation changes were observed in the martensite laths [51,52]. Fig. 5(d1)−(d3) show the IPF maps of the retained austenite. Together with Fig. 5(a1)−(a3), these results show that in the highlighted martensite regions most of the retained austenite grains had transformed into martensite. A statistical analysis of such regions shows that about 35% of the retained austenite in the analyzed region has undergone a TRIP effect at a global strain of 12.5%. Fig. 5(d1) also reveals that an apparent orientation difference exists in the retained austenite grains located in regions M+RA1 and M+RA2 (shown in Fig. 5(a1)). Since the crystal orientation of the retained austenite has been inherited from the prior austenite, these
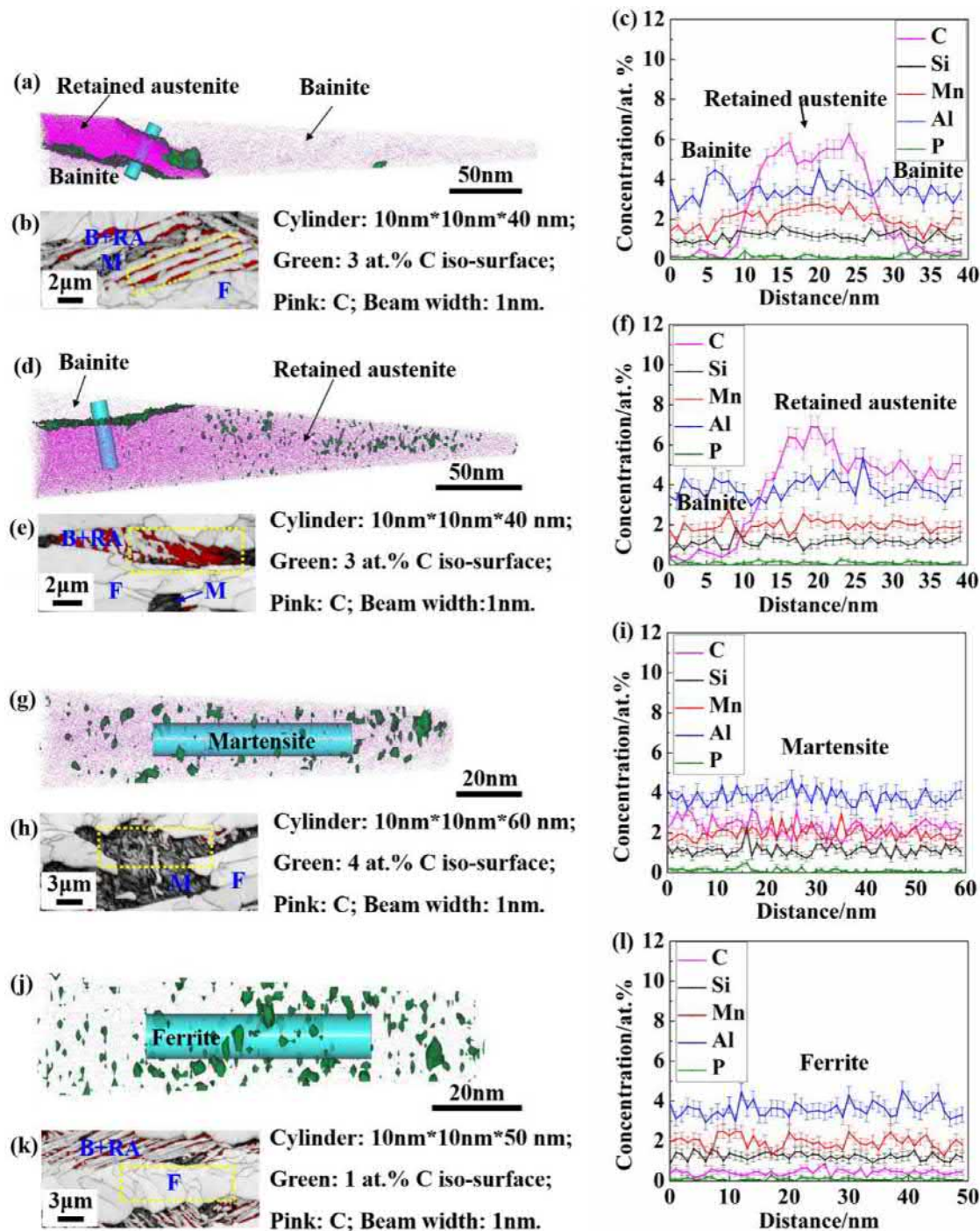
Fig. 3. APT results showing the element partition in the sample B (microstructure consisting of ferrite, bainite, martensite and retained austenite): (a) carbon map of the bainite and film-like retained austenite; (b) EBSD image quality map (with retained austenite in red) showing the local region (yellow rectangle) chosen for site-specific preparation of the APT tip shown in (a); (c) concentration profiles along the cylinder shown in (a); (d) carbon map of the bainite and blocky retained austenite; (e) EBSD image quality map showing the local region chosen for site-specific preparation of the APT tip shown in (d); (f) concentration profiles along the cylinder shown in (d); (g) carbon map of the martensite; (h) EBSD image quality map showing the local region chosen for site-specific preparation of the APT tip shown in (g); (i) concentration profiles along the cylinder shown in (g); (j) carbon map of the ferrite; (k) EBSD image quality map showing the local region chosen for site-specific preparation of the APT tip shown in (j); (l) concentration profiles along the cylinder shown in (j). All the concentrations are given in at.%. "F", "B", "M", and "RA" represent ferrite, bainite, martensite and retained austenite, respectively. (For interpretation of the references to colour in this figure legend, the reader is referred to the web version of this article.)

two *M*+RA regions should belong to different prior austenite grains, indicating the existence of a prior austenite grain boundary in the local martensite region highlighted by dashed rectangle. Fig. 5(e1)–(e3) show the Schmid factor maps for the {110}<111> slip systems of the bcc phase. The tensile deformation can result in an increase of the Schmid factor in the ferrite grain with relatively low initial Schmid factor. Fig. 5(f1)–(f3) give the Schmid factor maps for the

{111}<110> slip systems of the fcc phase. No substantial changes occur for the Schmid factors of the retained austenite during deformation.

Fig. 6 shows the quasi in-situ EBSD results for sample B. The image quality maps shown in Fig. 6(a1)–(a3) reveal that low index rate bands appear parallel to the bainite laths in both the ferrite and bainite with increasing global strain, as highlighted by
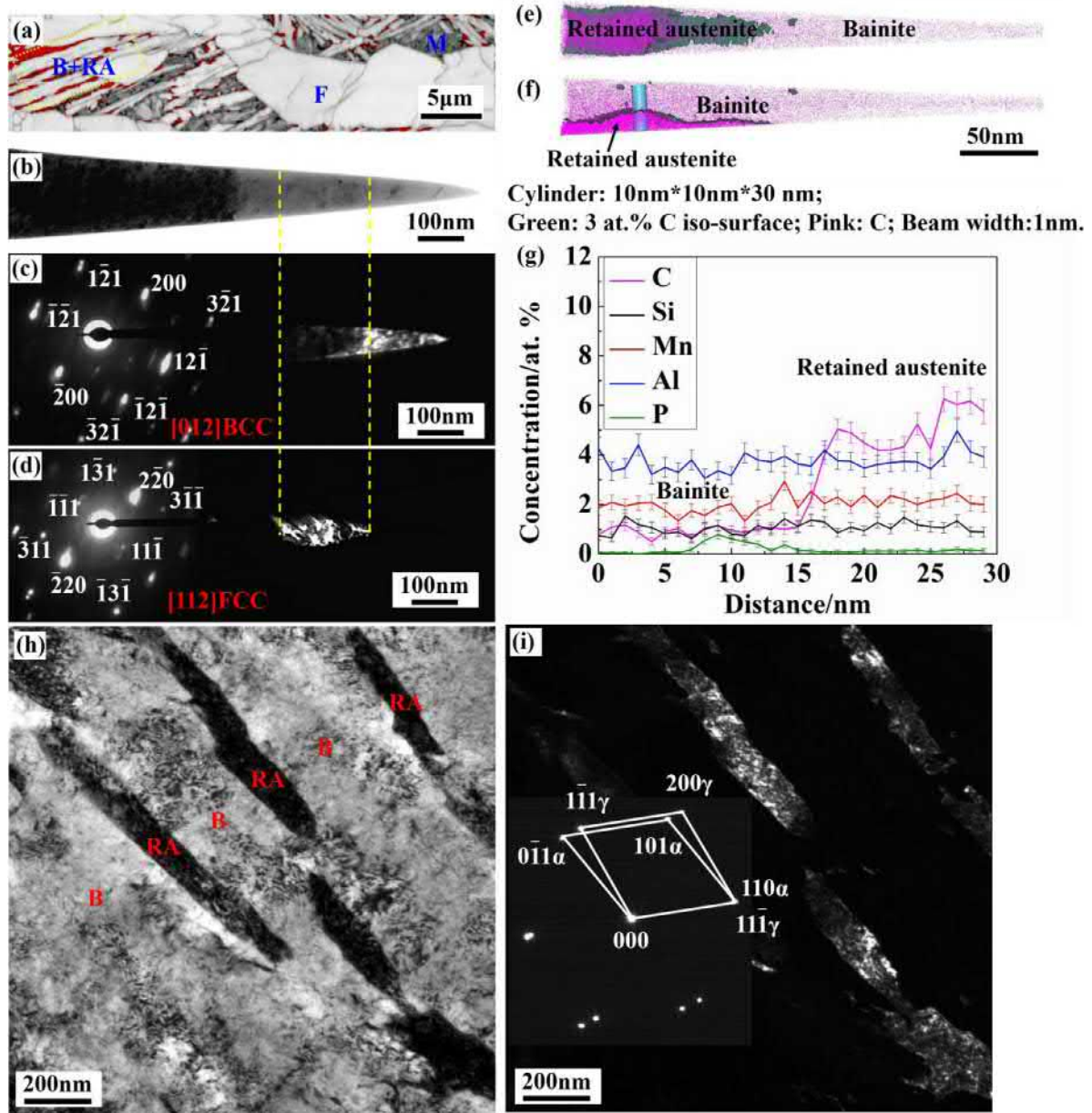
Fig. 4. Correlative TEM/APT measurements of sample B (microstructure consisting of ferrite, bainite, martensite and retained austenite): (a) EBSD image quality map showing the local region chosen for site-specific APT tip preparation; (b) bright field image of the APT tip; (c) dark field image of the bainite; (d) dark field image of the retained austenite; (e) (f) carbon map of the bainite and retained austenite; (g) concentration profiles along the cylinder shown in (f); (h) bright field image for the retained austenite and bainite; (i) dark field image for the retained austenite. All the concentrations are given in at.%. "F", "B", "M", and "RA" represent ferrite, bainite, martensite and retained austenite, respectively.

the dashed yellow rectangles. Some of the low index rate bands initiating in the ferrite region enter into the bainite region (highlighted by the yellow arrow). The grain boundary maps shown in Fig. 6(b1)−(b3) reveal that the density of the subgrain structures with 2−5° misorientation increases with higher global strain in the bainite and ferrite regions near the low index rate bands. These results indicate that strain localization in the form of bands form parallel to the bainite laths, both in the ferrite and bainite. Some of these bands penetrate from the ferrite into the bainite. Fig. 6(c1)−(c3) show the IPF maps of the bcc and fcc phases, revealing local orientation changes in both regions. Fig. 6 (d1)-(d3) show the IPF maps of the retained austenite. Comparing Fig. 6(d1) with Fig. 6(d3) reveals the TRIP effect. Nearly 55% of the retained austenite in the analyzed region shown in Fig. 6(d1) has been transformed by the TRIP effect at a global strain of 12.5%. Fig. 6(e1)−(e3) show the Schmid factor maps for the

{110}<111> slip systems of the bcc phase. The tensile deformation leads to an increase of the Schmid factor in the bainite lath with relatively low initial Schmid factor. The strain localization bands initiating in the ferrite enter into the bainite when their initial Schmid factors are both relatively high and close to each other. Fig. 6(f1)−(f3) give the Schmid factor maps for the {111}< 110> slip systems of the fcc phase. No substantial change occurs for the Schmid factor of the retained austenite during deformation.

Fig. 7 shows quantitative results of the strain contrast and strain partitioning between ferrite and martensite in sample M, obtained by μ-DIC analysis over a local region sized 20 μm × 20 μm. Fig. 7(a) shows an EBSD map of a representative region of interest prior to loading. Fig. 7(b)−(d) give the von Mises strain distribution of the same region at global strains of 4.2%, 8.3% and 12.5%, respectively, showing that the strain localizes in the ferrite. The martensite
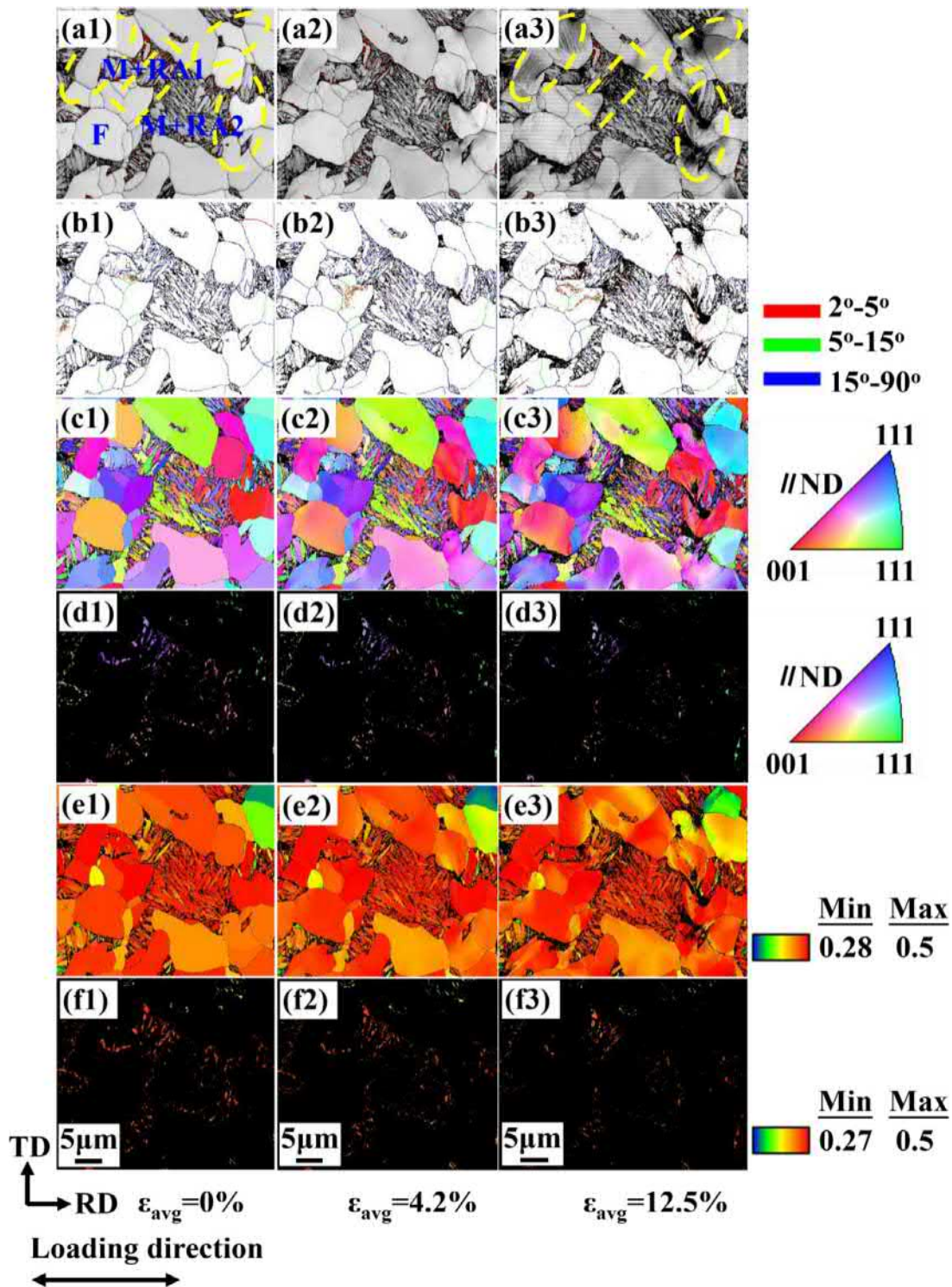
Fig. 5. Quasi in-situ EBSD results showing the deformation and TRIP effect in the sample M (microstructure consisting of ferrite, martensite and retained austenite): (a1)−(a3) EBSD image quality maps with retained austenite in red; (b1)-(b3) grain boundary maps (subgrain structures with 2−5° misorientation in red, low-angle grain boundaries with 5−15° misorientation in green, high-angle grain boundaries with 15−90° misorientation in blue); (c1)−(c3) IPF maps of both the bcc and fcc phases; (d1)−(d3) IPF maps of the fcc phase; (e1)−(e3) Schmid factor maps for the {110}<111> slip systems of the bcc phase; (f1)−(f3) Schmid factor maps for the {111}<110> slip systems of the fcc phase; (a1)(b1)(c1)(d1)(e1)(f1) ε_{avg}=0%; (a2)(b2)(c2)(d2)(e2)(f2) ε_{avg}=4.2%; (a3)(b3)(c3)(d3)(e3)(f3) ε_{avg}=12.5%. "F", "M", and "RA" represent ferrite, martensite and retained austenite, respectively. (For interpretation of the references to colour in this figure legend, the reader is referred to the web version of this article.)

remains essentially unstrained even at a global strain of 12.5%. Fig. 7 (e) and (f) provide the strain distribution along Sections 1 and 2, as indicated in Fig. 7(d), confirming the strong strain partitioning between ferrite and martensite. At a global strain of 12.5%, the local strain inside the ferrite reaches up to about 80% while that in the

martensite region is 2%−10%. The highest strain appears in the local ferrite region near the F/M interface. Fig. 7(g) shows statistical results about the strain partitioning between ferrite and martensite, obtained by averaging over 15−25 sections respectively in the ferrite and martensite. We find that the local strain in the ferrite region
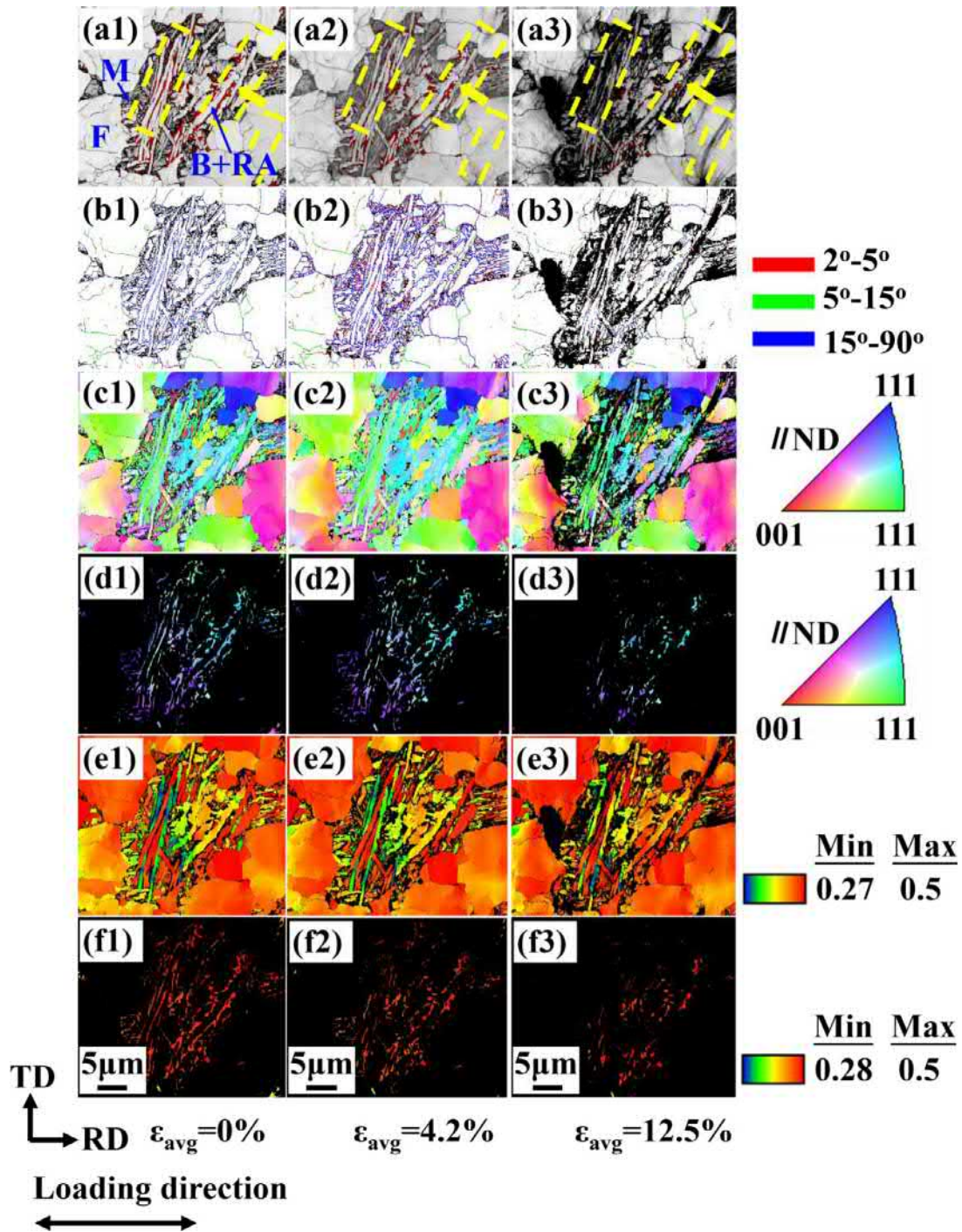
Fig. 6. Quasi in-situ EBSD results showing the deformation and TRIP effect in the sample B (microstructure consisting of ferrite, bainite, martensite and retained austenite): (a1)−(a3) EBSD image quality maps with retained austenite in red; (b1)−(b3) EBSD grain boundary maps (subgrain structures with 2−5° misorientation in red, low-angle grain boundaries with 5−15° misorientation in green, high-angle grain boundaries with 15−90° misorientation in blue); (c1)-(c3) IPF maps of both the bcc and fcc phases; (d1)-(d3) IPF maps of the fcc phase; (e1)-(e3) Schmid factor maps for the {110}<111> slip systems of the bcc phase; (f1)-(f3) Schmid factor maps for the {111}<110> slip systems of the fcc phase; (a1)(b1)(c1)(d1)(e1)(f1) ε_{avg}=0%; (a2)(b2)(c2)(d2)(e2)(f2) ε_{avg}=4.2%; (a3)(b3)(c3)(d3)(e3)(f3) ε_{avg}=12.5%. "F", "B", "M", and "RA" represent ferrite, bainite, martensite and retained austenite, respectively. (For interpretation of the references to colour in this figure legend, the reader is referred to the web version of this article.)

increases much faster than that in the martensite region with increasing load. In the ferrite, strain is distributed much more inhomogeneously than in the martensite.

To evaluate the relationship between the strain partitioning and the TRIP effect in material M, a combined μ-DIC and EBSD analysis was performed, Fig. 8. Five tensile steps, accumulating to a total global strain of 20.8%, were imposed to initiate the TRIP effect. Fig. 8 (a) shows the microstructure prior to loading. Fig. 8(b)−(d) give the

von Mises strain distribution of the same region at global strains of 4.2%, 8.3% and 20.8%, respectively, revealing the strong strain localization inside the ferrite. Comparing the microstructure at a global strain of 20.8% (Fig. 8(e)) with that prior to loading (Fig. 8(a)), we find that the retained austenite located in the strain localized martensite regions, near the F/M interfaces, performed a TRIP effect. Fig. 8(f)−(h) provide the strain distribution along Sections 1−3, as shown in Fig. 8 (d), revealing the strong strain contrast between ferrite and
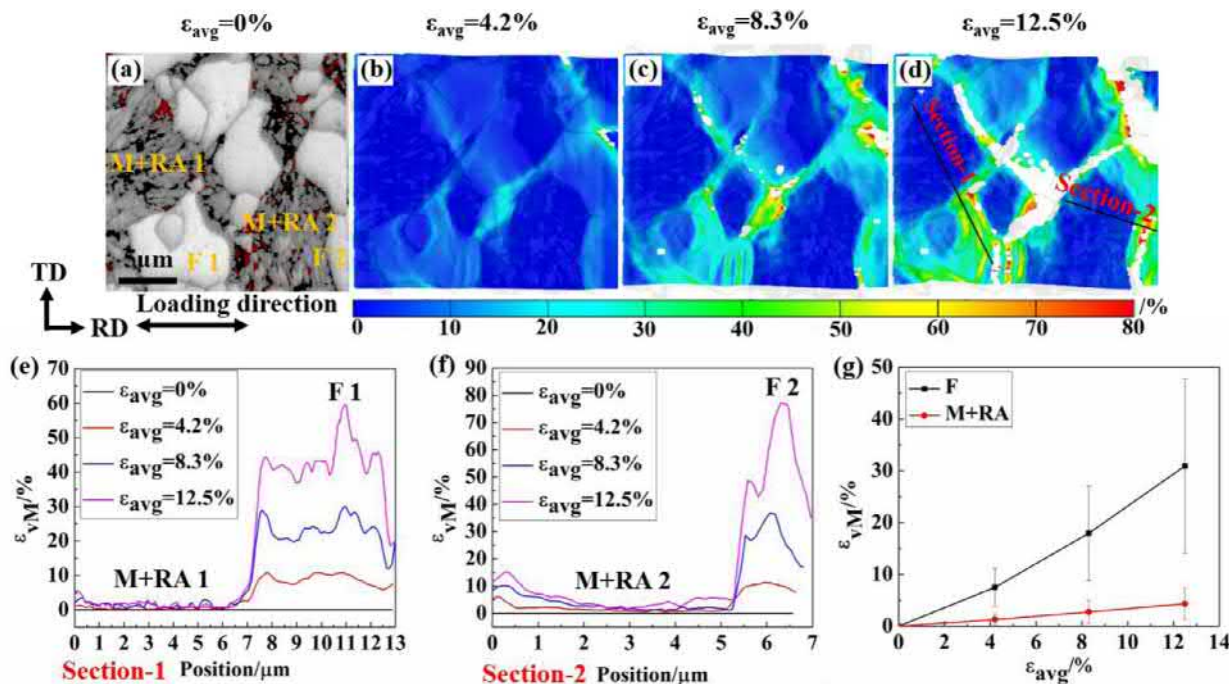
Fig. 7. Quasi in-situ μ-DIC analysis results showing the strain contrast and strain partitioning between the ferrite and martensite regions in the sample M (microstructure consisting of ferrite, martensite and retained austenite): (a) EBSD image quality map with retained austenite in red for the microstructure without deformation; (b) von Mises strain map of the local region at a global strain of 4.2%; (c) von Mises strain map of the local region at a global strain of 8.3%; (d) von Mises strain map of the local region at a global strain of 12.5%; (e) von Mises strain contrast along the section-1; (f) von Mises strain contrast along the section-2; (g) von Mises strain partitioning between the ferrite and martensite regions. "F", "M" and "RA" represent ferrite, martensite and retained austenite, respectively. (For interpretation of the references to colour in this figure legend, the reader is referred to the web version of this article.)

martensite. At a global strain of 20.8%, the strain difference between the ferrite and martensite can reach up to about 50%, as shown in Fig. 8(g). Fig. 8(i) shows the statistical results of the strain partitioning between the ferrite and martensite, obtained by averaging over 15−25 sections respectively in the ferrite and martensite. The ferrite exhibits larger average strain and stronger strain inhomogeneity than the martensite. The strain partitioning results of the ferrite grains, Fig. 8(j), indicate that the local strain in the narrow ferrite regions (F1, F3 and F5) located between two martensite regions is much larger than that in the ferrite regions (F2, F4 and F6) which are encompassed and protected by interconnected martensite regions. The strain partitioning results of the martensite, shown in Fig. 8(k), reveal that the martensite regions (M+RA4 and M+RA5) located near the strain localized ferrite exhibit higher local strain than the other martensite regions (M+RA1, M+RA2 and M+RA3).

Fig. 9 shows the strain contrast and partitioning between ferrite and bainite in material B. Fig. 9(a) provides the microstructure in undeformed state. Fig. 9(b)−(d) reveal the von Mises strain distribution in the same region at global strains of 4.2%, 8.3% and 12.5%. We find that strain localization bands appear parallel to the bainite laths in both the ferrite and bainite with increasing global strain. Some strain localization bands initiating in the ferrite can enter into the bainite, coinciding with the EBSD results shown in Fig. 6. This phenomenon is attributed to the fact that plastic slip is triggered inside of the bainite when the local load is high enough. Fig. 9(e) and (f) give the strain distribution along Sections 1 and 2, as shown in Fig. 9 (d), revealing much lower strain contrast between ferrite and bainite, compared with that between the ferrite and martensite in sample M. At a global strain of 12.5%, the local strain in ferrite and bainite is, respectively, 1%−12% and 1%−14%. Fig. 9(g) shows the strain partitioning results between the ferrite and bainite. We find that the average local strain in the ferrite is larger than that in the bainite. The local strain in the ferrite increases faster than that in the bainite with increasing global strain. Fig. 9(g) also shows that the average local strain in both the ferrite and bainite are lower than the global strain.

It is attributed to the macroscopically inhomogeneous distribution of the strain in the sample.

Fig. 10 shows the strain contrast and strain partitioning among ferrite, bainite and martensite in sample B. Fig. 10(a) shows the microstructure in the undeformed state. Fig. 10(b)−(d) present the von Mises strain distribution of the same region at global strains of 4.2%, 8.3% and 12.5%, indicating the strong strain localization in ferrite and bainite and the distinct strain contrast between ferrite and martensite. The microstructure of the local region at global strain of 12.5%, Fig. 10(e), shows that the retained austenite highlighted by the white arrows have performed the TRIP effect during the deformation. However, the local strain of the highlighted sites is still lower than that in the ferrite. Fig. 10(f) and (g) provide the strain distribution along the Sections 1 and 2, as indicated in Fig. 10(d), revealing that the strain contrast between ferrite and martensite is much stronger than that between ferrite and bainite. At a global strain of 12.5%, the local strain in ferrite, bainite and martensite is, respectively, 10%−50%, 2−23% and 2%−5%. Strain localization also exists in the bainite near the B/M interface. Fig. 10(h) shows the strain partitioning between the ferrite, bainite and martensite regions. The strain in the material is mainly partitioned into the ferrite and bainite, especially ferrite. The local strain in the ferrite and bainite increases much faster than that in the martensite. Moreover, the ferrite and bainite exhibit more pronounced strain inhomogeneities than the martensite.

4. Discussion

4.1. Effect of carbon partitioning on stability features of retained austenite

As the APT results show, the carbon partitioning can result in a carbon gradient in the retained austenite. This means that correspondingly a stability gradient exists in the retained austenite, since austenite stabilization depends in the present system mainly on the carbon content. Retained austenite can perform different
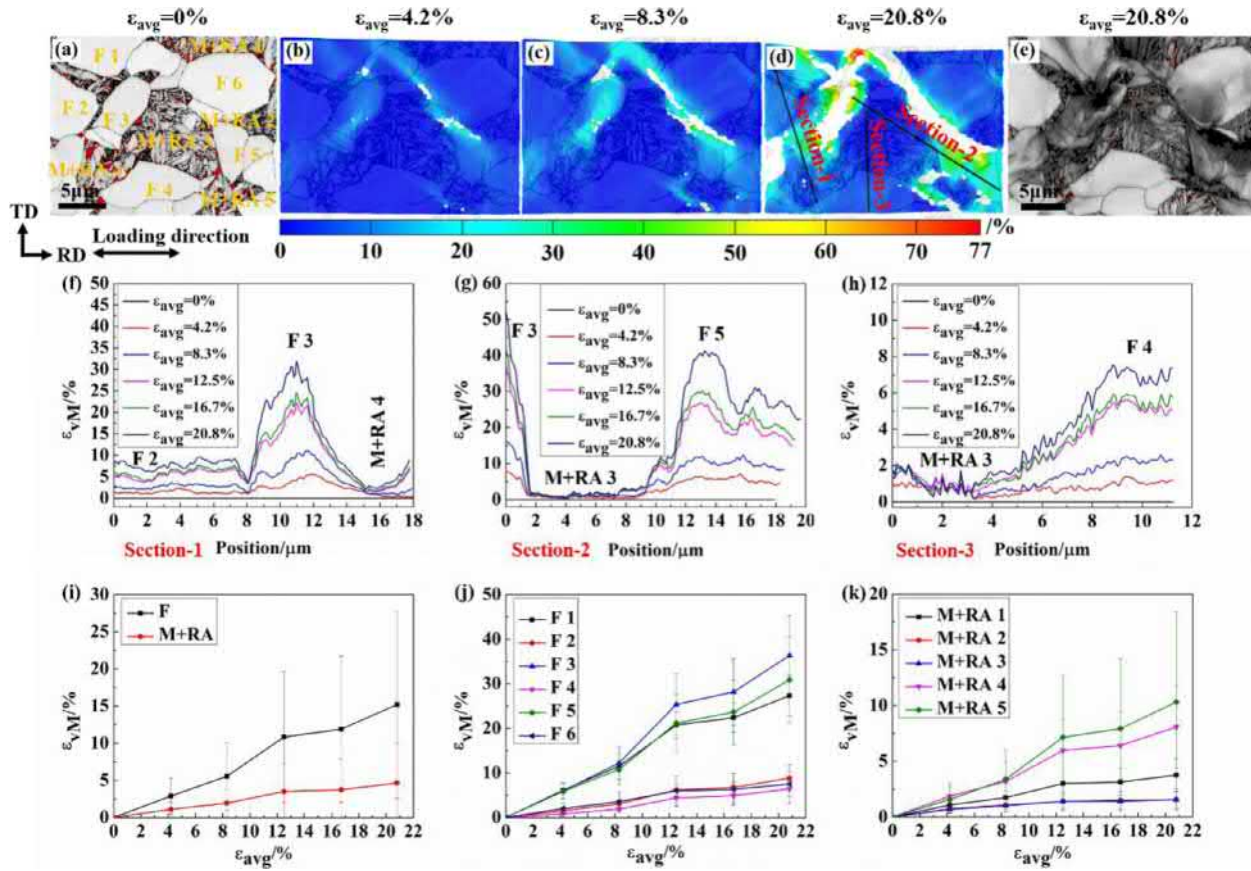
Fig. 8. Quasi in-situ μ-DIC analysis results showing the strain contrast and strain partitioning between the ferrite and martensite regions in the sample M (microstructure consisting of ferrite, martensite and retained austenite): (a) EBSD image quality map with retained austenite in red for the microstructure without deformation; (b) von Mises strain map of the local region at a global strain of 4.2%; (c) von Mises strain map of the local region at a global strain of 8.3%; (d) von Mises strain map of the local region at a global strain of 20.8%; (e) EBSD image quality map with retained austenite in red for microstructure at a global strain of 20.8%; (f) von Mises strain contrast along the section-1; (g) von Mises strain contrast along the section-2; (h) von Mises strain contrast along the section-3; (i) von Mises strain partitioning between the ferrite and martensite regions; (j) von Mises strain partitioning among the ferrite grains; (k) von Mises strain partitioning among the martensite regions. "F", "M" and "RA" represent ferrite, martensite and retained austenite, respectively. (For interpretation of the references to colour in this figure legend, the reader is referred to the web version of this article.)
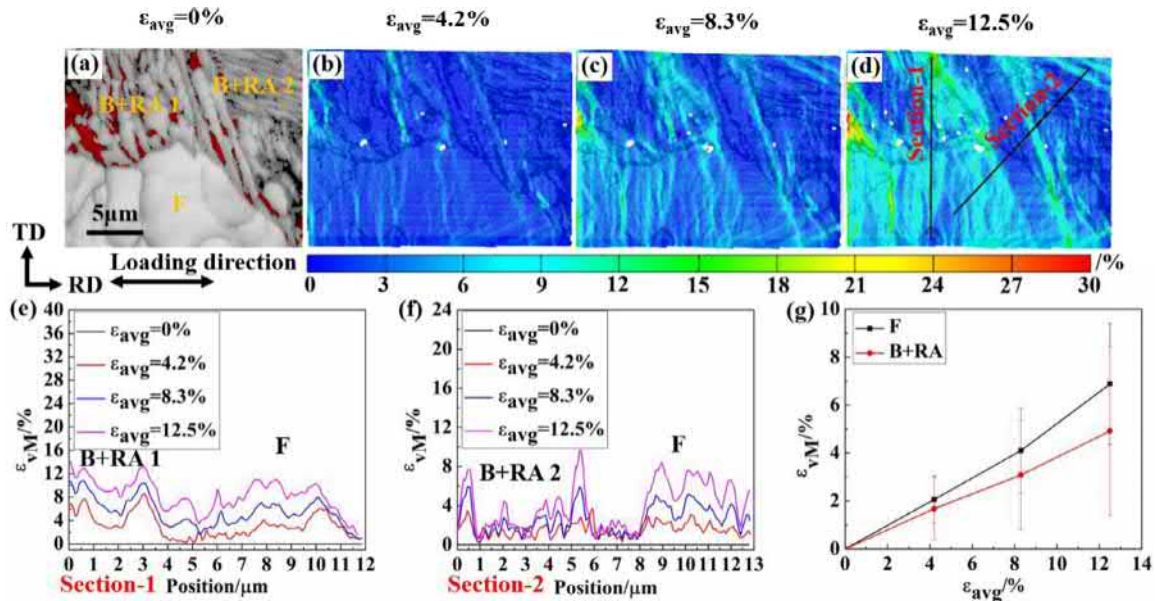

Fig. 9. Quasi in-situ μ-DIC analysis results showing the strain contrast and strain partitioning between the ferrite and bainite regions in the sample B (microstructure consisting of ferrite, bainite, martensite and retained austenite): (a) EBSD image quality map with retained austenite in red for the microstructure without deformation; (b) von Mises strain map of the local region at a global strain of 4.2%; (c) von Mises strain map of the local region at a global strain of 8.3%; (d) von Mises strain map of the local region at a global strain of 12.5%; (e) von Mises strain contrast along the section-1; (f) von Mises strain contrast along the section-2; (g) von Mises strain partitioning between the ferrite and bainite regions. "F", "B" and "RA" represent ferrite, bainite and retained austenite, respectively. (For interpretation of the references to colour in this figure legend, the reader is referred to the web version of this article.)
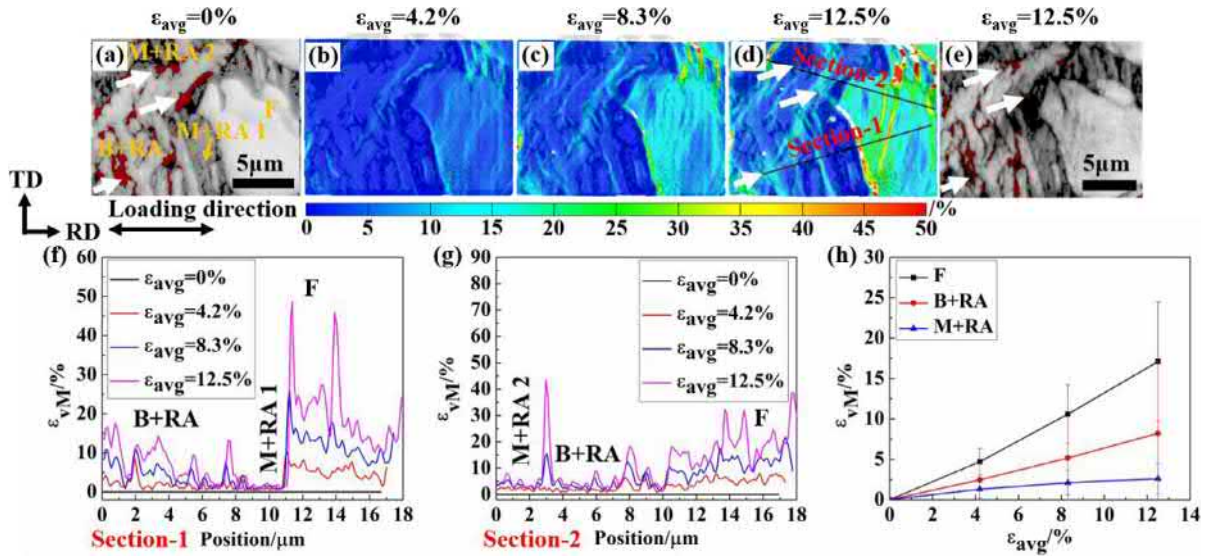
Fig. 10. Quasi in-situ μ-DIC analysis results showing the strain contrast and strain partitioning among the ferrite, bainite and martensite regions in sample B (microstructure consisting of ferrite, bainite, martensite and retained austenite): (a) EBSD image quality map with retained austenite in red for the microstructure without deformation; (b) von Mises strain map of the local region at a global strain of 4.2%; (c) von Mises strain map of the local region at a global strain of 8.3%; (d) von Mises strain map of the local region at a global strain of 12.5%; (e) EBSD image quality map with retained austenite in red for microstructure at a global strain of 12.5%; (f) von Mises strain contrast along the section-1; (g) von Mises strain contrast along the section-2; (h) von Mises strain partitioning among the ferrite, bainite and martensite regions. "F", "B", "M" and "RA" represent ferrite, bainite, martensite and retained austenite, respectively. (For interpretation of the references to colour in this figure legend, the reader is referred to the web version of this article.)

deformation mechanisms, such as dislocation glide, mechanical twinning and martensitic transformation, depending on the stacking fault energy (SFE) controlled by the chemical composition [53–55]. With decreasing SFE, the active plasticity mode follows a sequence of dislocation glide, mechanical twinning and martensitic transformation. TRIP sets in when the SFE is below 18 mJ/m^2 and the TWIP effect prevails when the SFE is between 18 mJ/m^2 and 45 mJ/m^2 [56]. Previous XRD results show, for the material studied here, that the average carbon concentration in the retained austenite is 1.05−1.08 wt.% (about 4.76−4.85 at.%) and retained austenite with a carbon content above 1.30 wt.% (about 5.79 at.%) was shown to not undergo a martensitic transformation when exposed to tensile loads [16]. To investigate the prevalent deformation mechanism of the retained austenite, we calculated the SFE using the Olson-Cohen thermodynamic model based on the APT measured concentration profiles [57]. The ideal SFE, γSFE, is expressed as Eq. (1) [58]:

$$\gamma_{SFE} = 2\rho\Delta G^{\gamma\rightarrow\varepsilon} + 2\sigma \tag{1}$$

where ρ is the molar surface density along {111} planes, $\Delta G^{\gamma\rightarrow\varepsilon}$ is the molar Gibbs energy of the austenite to ε-martensite phase transformation and σ is the interfacial energy per unit area of the phase boundary, which was assumed to be $\sigma = 8$ mJ/m^2 [58]. The molar surface density ρ can be calculated based on the austenite lattice parameter a and Avogadro's constant N using Eq. (2) [56]:

$$\rho = \frac{4}{\sqrt{3}}\frac{1}{a^2N} \tag{2}$$

The molar Gibbs energy of the austenite to ε-martensite phase transformation $\Delta G^{\gamma\rightarrow\varepsilon}$ is calculated according to Eq. (3) [57]:

$$\begin{aligned}\Delta G^{\gamma\rightarrow\varepsilon} = &X_{Fe}\Delta G_{Fe}^{\gamma\rightarrow\varepsilon} + X_{Mn}\Delta G_{Mn}^{\gamma\rightarrow\varepsilon} + X_{Al}\Delta G_{Al}^{\gamma\rightarrow\varepsilon}\\&+ X_{Si}\Delta G_{Si}^{\gamma\rightarrow\varepsilon} + X_C\Delta G_C^{\gamma\rightarrow\varepsilon} + X_{Fe}X_{Mn}\Omega_{FeMn}^{\gamma\rightarrow\varepsilon}\\&+ X_{Fe}X_{Al}\Omega_{FeAl}^{\gamma\rightarrow\varepsilon} + X_{Fe}X_{Si}\Omega_{FeSi}^{\gamma\rightarrow\varepsilon}\\&+ X_{Fe}X_C\Omega_{FeC}^{\gamma\rightarrow\varepsilon} + X_{Mn}X_C\Omega_{MnC}^{\gamma\rightarrow\varepsilon} + \Delta G_{mg}^{\gamma\rightarrow\varepsilon}\end{aligned} \tag{3}$$

where X_i and $\Delta G_i^{\gamma\rightarrow\varepsilon}$ show the molar fraction and free energy change due to a hcp martensite formation from fcc austenite in pure metals,

respectively. $\Omega_{ij}^{\gamma\rightarrow\varepsilon}$ is the interaction energy between the components i and j. $\Delta G_{mg}^{\gamma\rightarrow\varepsilon}$ is the free energy contribution due to the magnetic transition. The thermodynamic values and functions used to calculate the $\Delta G^{\gamma\rightarrow\varepsilon}$ are listed in Table 1.

To partly reveal the thermal stability of the retained austenite, we also calculated the martensite start (M$_s$) temperature using Eq. (4) [16]:

$$M_s(^\circ C) = 545 - 423C - 30.4Mn - 7.5Si + 30Al - 60.5V_\gamma^{-1/3} \tag{4}$$

where C, Mn, Si and Al are the concentrations of these elements in wt.%. and V_γ is the average austenite grain volume in μm^3, assumed as 0.2 μm^3. Fig. 11 gives the calculated SFE and M$_s$ temperature of retained

Table 1
Thermodynamics-based values and functions used to calculate the $\Delta G^{\gamma\rightarrow\varepsilon}$ [53,55–59]. T is the temperature in K; G$_{mg}^\varphi$ is the magnetic contribution to the Gibbs energy of phase φ, $\varphi = \gamma$, ε; β^φ, T$_N^\varphi$ and μ$_B$ are the magnetic moment, the Néel temperature of phase φ and the Bohr magneton, respectively; R is the gas constant; P is the fraction of magnetic enthalpy absorbed above T$_N^\varphi$; τ is the scaled Néel temperature.

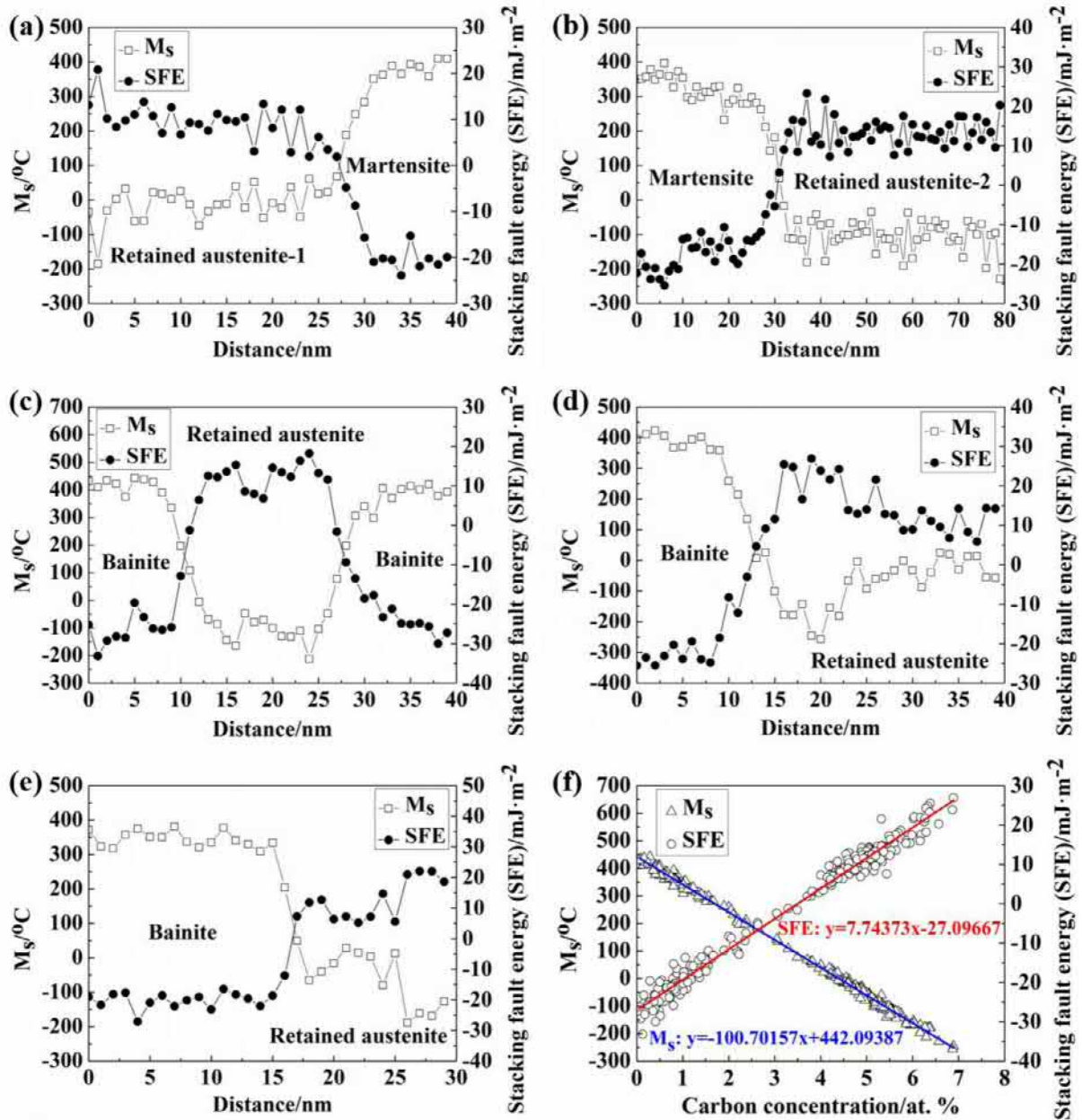| Parameter	Values and functions
$\Delta G_{Fe}^{\gamma\rightarrow\varepsilon}$/J•mol^{-1}	−2343.38+4.309T
$\Delta G_{Mn}^{\gamma\rightarrow\varepsilon}$/J•mol^{-1}	−1000.00+1.123T
$\Delta G_{Al}^{\gamma\rightarrow\varepsilon}$/J•mol^{-1}	2800+5T
$\Delta G_{Si}^{\gamma\rightarrow\varepsilon}$/J•mol^{-1}	−560−8T
$\Delta G_C^{\gamma\rightarrow\varepsilon}$/J•mol^{-1}	−24,595.12
$\Omega_{FeMn}^{\gamma\rightarrow\varepsilon}$/J•mol^{-1}	−9135.5 + 15,282.1X$_{Mn}$
$\Omega_{FeAl}^{\gamma\rightarrow\varepsilon}$/J•mol^{-1}	3328
$\Omega_{FeSi}^{\gamma\rightarrow\varepsilon}$/J•mol^{-1}	2850+3520(X$_{Fe}$-X$_{Si}$)
$\Omega_{FeC}^{\gamma\rightarrow\varepsilon}$/J•mol^{-1}	42,500
$\Omega_{MnC}^{\gamma\rightarrow\varepsilon}$/J•mol^{-1}	26,910
$\Delta G_{mg}^{\gamma\rightarrow\varepsilon}$	$\Delta G_{mg}^{\gamma\rightarrow\varepsilon}$ =G$_{mg}^\varepsilon$-G$_{mg}^\gamma$
ΔG_{mg}^φ	$f(T/T_N^\varphi)$RTln(1+β^φ/μ$_B$), $\varphi = \gamma$, ε
$f(T/T_N^\varphi)$	1-[79τ^{-1}/140 P + 474/497(1/P-1)(τ^3/6+τ^9/135+τ^{15}/600)]/ D, when $\tau \leq 1$ ($\tau = T/T_N^\varphi$); -(τ^{-5}/10+τ^{-15}/315+τ^{-25}/ 1500)/D, when $\tau > 1$; P = 0.28
D	518/1125+11,692/15,975(1/P-1), P = 0.28
β^γ/μ$_B$/J•mol^{-1}	0.7X$_{Fe}$+0.62X$_{Mn}$−0.64X$_{Fe}$X$_{Mn}$−4X$_C$
β^ε/μ$_B$/J•mol^{-1}	0.62X$_{Mn}$−4X$_C$
T$_N^\gamma$/K	251.71+681X$_{Mn}$−1575X$_{Si}$−1740X$_C$
T$_N^\varepsilon$/K	580X$_{Mn}$

Fig. 11. Calculated stacking fault energy (SFE) and martensite start (M$_s$) temperature of retained austenite based on the concentration profiles measured by APT: (a), (b), (c), (d) and (e) are the calculation results for the profiles shown in Fig. 2(c), Fig. 2(d), Fig. 3(c), Fig. 3(f) and Fig. 4(g), respectively; (f) shows the relation among SFE, M$_s$ and carbon concentration in the austenite

austenite basing on the APT concentration profiles shown in Figs. 2−4. Fig. 11(a)−(e) show that the SFE is between 3 mJ/m^2 and 27 mJ/m^2 and the M$_s$ temperature is in the range of −245−25 °C. We can see that the inhomogeneous distribution of carbon in the retained austenite can result in huge fluctuations of SFE and M$_s$ temperature. The retained austenite with higher carbon concentration exhibits higher SFE and lower M$_s$ temperature. Fig. 11(f) reveals that the relation between the SFE and carbon concentration can be approximated by Eq. (5), and that between M$_s$ temperature and carbon concentration by Eq. (6), where x$_C$ is the carbon concentration in at.%. Since the SFE value of 18 mJ/m^2 is the upper limit for triggering the TRIP effect, retained austenite with a carbon concentration below 5.82 at.% (about 1.31 wt.%) can undergo a TRIP effect, according to Eq. (5). The SFE of the retained austenite with a carbon concentration of 5.82−7.00 at.% (about 1.31−1.59 wt.%) is in the range

of 18−27 mJ/m^2, thus it is more likely to deform via TWIP. This can partly explain why retained austenite regions with a carbon concentration above 1.30 wt.% prevail when exposed to tensile loading [16]. Eq. (6) shows that retained austenite with a M$_s$ temperature below 25 °C should possess a carbon concentration of at least 4.14 at.% (about 0.92 wt.%) or higher. In summary, enhancing the TRIP effect in retained or reversed austenite in the current material requires to increase its carbon concentration to levels of 4.14−5.82 at.% (about 0.92−1.31 wt.%) through carbon partitioning.

$$\gamma_{SFE}\left(mJ/m^2\right) = 7.74373x_C(at.\%) - 27.09667\gamma_{SFE}\left(mJ/m^2\right)$$

$$= 7.74373x_C(at.\%) - 27.09667 \tag{5}$$

$$M_s(\,°C) = -100.70157x_C(at.\%) + 442.09387 \tag{6}$$

4.2. Effect of strain partitioning on TRIP effect and ductility

For multiphase materials, plastic instabilities, strain localization and fracture are related to local inhomogeneities in the size, distribution, morphology, dislocation density and chemical composition of the phases and microstructure constituents [7,12,34,60]. As the μ-DIC results show, significant differences in the deformation behavior exist between the two materials types M and B, specifically regarding micro-yielding, strain partitioning and strain localization. For material type M with its microstructure consisting of ferrite, martensite and retained austenite, deformation starts in the soft ferrite. Except for some modest strain enhancement in the martensite regions near the F/M interfaces and prior austenite grain boundaries, the strain is mainly partitioned into the ferrite. Bands of localized strain form in the ferrite, but they do not penetrate into the martensite regions. This leads to negligible deformation of the martensite and pronounced strain contrast at the F/M interfaces. Since the retained austenite triggers the TRIP effect only above a critical deformation level, low local strain concentrations thus leads to a very weak TRIP effect [22,61−63]. The strong strain localization in the local ferrite regions near the F/M interfaces can accelerate the crack initiation at the interfaces [20]. The priority for the crack propagation along the interfaces finally promotes the fracture of the material [15]. These results show that the strain partitioning among the main microstructure constituents controls three important factors that govern the formability of ferrite-containing TRIP-assisted steel, namely, strain localization and damage initiation, ferrite deformation and the intensity and distribution of the TRIP effect.

Comparing the strain partitioning results observed for material B (ferrite, bainite, martensite, retained austenite) with those of material M (ferrite, martensite, retained austenite), shows that the introduction of bainite can effectively improve the deformation homogeneity of the steel. At the onset of plastic yielding, deformation begins both in the ferrite and in the bainite. With a hardness of 391 ± 33 HV, the bainite has a strength that lies between that of the ferrite (213 ± 16 HV) and the martensite (542 ± 41 HV). Thus, this constituent acts as a mechanical buffer and compliance zone between the soft and hard regions of the microstructure. The presence of bainite in material B effectively reduces the area fraction of F/M interfaces, compared to material M. This effect reduces the appearance of strong strain contrast at these interfaces, as shown in Figs. 9 and 10. The lower hardness difference between the ferrite and bainite (about 178 HV) leads to a modest strain contrast at the F/B interfaces, with a strain difference of about 8%−27%. Distinct strain contrast also exists at the B/M interfaces, yet, with a lower strain difference of about 3%−18%, below that at the F/M interfaces, Figs. 8 and 10. The lower average strain contrast in the bainite containing microstructures reduces strain localization and crack initiation at interfaces and shifts the deformation from the interface regions into the ferrite and bainite regions, thus improving ductility. The intermediate deformation of the bainite promotes strain transfer from the matrix to the retained austenite, thus enhancing the TRIP effect. The term "strain transfer" refers here to the observation that the deformation of the retained austenite can be triggered when the local strain in its surrounding matrix (bainite or martensite) reaches a certain level. The quasi in-situ EBSD (Fig. 6) and μ-DIC (Fig. 9) results show that some of the strain localization bands initiated in the ferrite regions enter into bainite regions, increasing the deformation of the bainite. The strain and EBSD patterns shown in Fig. 10 reveal that the TRIP effect in the retained austenite is indeed triggered by strain localization in the adjacent bainite. Although some of the retained austenite has performed a TRIP effect, the correspondingly enhanced strain peaks at the transformed regions is still lower than the local strain in the ferrite or bainite regions. This means that the main origin of the ductility of material B is not the TRIP effect alone but the reduction in strain localization and by the deformation carried by the ferrite and bainite.

Since the volume fraction and strain level of the ferrite are similar in samples M and B, the deformation of the bainite can be regarded as a crucial factor resulting in the higher formability of sample B.

4.3. Property optimization based on carbon and strain partitioning control

The discussion above shows that the ductility of multiphase TRIP steels is improved when composing the matrix surrounding the retained austenite islands of ferrite, bainite and martensite. This is attributed to the reduction in pronounced interfacial strain localization and microcracking, modest strain partitioning which is mainly realized through the presence of bainite, and the TRIP effect. These effects all originate from bolstering the strength contrast among the microstructure constituents which in turn regulate strain partitioning. Here lies an important relationship between mechanical and chemical partitioning since it is mainly the different carbon content and the resulting substructure hierarchy that governs the strength relationship among of the individual microstructure constituents [48,64]. Thus, tuning strain homogeneity in a multiphase steel requires adjustment of the strength contrast among the constituents by controlling carbon partitioning and the resulting substructure. The APT results showed that the substitutional elements such as Mn, Al and Si are less relevant in this context as they do not partition, Figs. 2−4. For the specific case of TRIP-assisted multiphase steels the carbon plays a complex role: The carbon content and its partitioning behavior determine the (i) stability of the retained austenite and hence the onset and progression of the TRIP effect upon loading, (ii) the strength and substructure of the bainite and (iii) the strength and substructure of the martensite. The DIC and EBSD maps (Figs. 7−10) have shown that this relationship between mechanical and chemical partitioning effects is non-linear, i.e. the strength contrast among the matrix constituents affects the strain partitioning and thus also the local load transfer acting on the retained austenite, triggering the TRIP effect.

This means that multiphase TRIP steel design requires to not only tune the amount and stability of the retained austenite islands in terms of their carbon concentration, size, morphology, distribution and crystal orientation, but also to consider the mechanical partitioning of the strain among the austenite and surrounding mixed constituent matrix ingredients with the aim to enhance strain transfer into the retained austenite. As found in the analysis of material M, low uniform elongation and a weak TRIP effect mainly result from the high strength contrast between the ferrite and martensite, leading to a low strain in the martensite regions. Material B reveals that this effect can be bolstered through the addition of bainite as a load and strain buffer rendering the strain partitioning less abrupt. Another important factor affecting the interplay between mechanical and chemical partitioning is the size and dispersion of the retained austenite which determines the time required for carbon to sweep the grains and at the same time affects the nucleation rate of the TRIP effect when mechanically loaded. The carbon content also affects the packet size and lath structure of the martensite, two factors which govern its strength and the resulting load transfer to its neighbor constituents. This can be further altered by the tempering state of the martensite.

5. Conclusions

The target of this work was to obtain a better understanding of the interplay between chemical (carbon) and mechanical partitioning in multiphase TRIP steels. We applied two hot rolling direct quenching and partitioning (HDQ&P) processes to a low-C low-Si Al-added steel and obtained two types of ferrite-containing TRIP-assisted steels with different constituents, one with ferrite, bainite, martensite and retained austenite and a second one with ferrite, martensite and

retained austenite. We used APT to investigate the carbon partitioning among the microstructure constituents at the near-atomic-scale. The strain partitioning and the TRIP effect were investigated using quasi in-situ tensile test combined with μ-DIC and EBSD mapping. The combination of these results enabled us to propose a property optimization strategy for ferrite-containing TRIP-assisted steels based on carbon and strain partitioning control. The main results and conclusions are:

(1) The carbon is distributed inhomogeneously in retained austenite, i.e. with differences between different retained austenite islands and with carbon concentration gradients inside individual islands. The HDQ&P processes leaves Si, Mn, Al and P un-partitioned among all microstructure constituents, i.e. ferrite, martensite, bainite and retained austenite.

(2) For multiphase TRIP-assisted steels, the pronounced strength difference between the soft and hard matrix structures can result in pronounced strain localization in the soft phase. Low strain in the hard constituents reduces load transfer and thus the effectiveness of the TRIP effect in the retained austenite. The strong strain contrast at the interfaces between the soft and hard phases can promote interfacial fracture.

(3) The deformation of the soft ferrite enhances ductility of ferrite-containing TRIP-assisted steels. The TRIP effect does not directly result in local strain spikes, but together with the increase in the strain hardening rate, it can increase the average strain in the hard-matrix thus reducing strain contrast at the interfaces between the soft and hard phases. This effect delays crack initiation.

(4) Optimizing the TRIP effect in multiphase TRIP steel requires to not only tune the amount and stability of the retained austenite islands in terms of their carbon concentration, size, morphology, distribution and crystal orientation, but also to consider the mechanical partitioning of the strain among the austenite and its surrounding mixed constituent matrix ingredients with the aim to enhance strain transfer into the retained austenite.

Declaration of Competing Interest

The authors declare that they have no known competing financial interests or personal relationships that could have appeared to influence the work reported in this paper.

Acknowledgments

References

[1] M.J. Santofimia, T. Nguyen-Minh, L. Zhao, R. Petrov, I. Sabirov, J. Sietsma, New low carbon Q&P steels containing film-like intercritical ferrite, Mat. Sci. Eng. A Struct. 527 (2010) 6429–6439.

[2] T.Y. Hsu Xu Zuyao, X.J. Jin, Y.H. Rong, Strengthening and toughening mechanisms of quenching-partitioning-tempering (Q-P-T) steels, J. Alloy Compd. 5771 (2013) S568–S571.

[3] E.J. Seo, L. Cho, Y. Estrin, B.C. De Cooman, Microstructure-mechanical properties relationships for quenching and partitioning (Q&P) processed steel, Acta Mater 113 (2016) 124–139.

[4] B.C. De Cooman, Structure-properties relationship in trip steels containing carbide-free bainite, Curr. Opin. Solid St M. 8 (2004) 285–303.

[5] J. Speer, D.K. Matlock, B.C. De Cooman, J.G. Schroth, Carbon partitioning into austenite after martensite transformation, Acta Mater 51 (2003) 2611–2622.

[6] J.G. Speer, D.V. Edmonds, F.C. Rizzo, D.K. Matlock, Partitioning of carbon from supersaturated plates of ferrite, with application to steel processing and fundamentals of the bainite transformation, Curr. Opin. Solid St M 8 (2004) 219–237.

[7] M.M. Wang, C.C. Tasan, D. Ponge, D. Raabe, Spectral trip enables ductile 1.1GPa martensite, Acta Mater 111 (2016) 262–272.

[8] Z.H. Cai, H. Ding, R.D.K. Misra, Z.Y. Ying, Austenite stability and deformation behavior in a cold-rolled transformation-induced plasticity steel with medium manganese content, Acta Mater 84 (2015) 229–236.

[9] J.G. Speer, E. De Moor, A.J. Clarke, Critical assessment 7: quenching and partitioning, Mater Sci. Tech-Lond. 31 (2015) 3–9.

[10] S. Zhang, K.O. Findley, Quantitative assessment of the effects of microstructure on the stability of retained austenite in TRIP steels, Acta Mater 61 (2013) 1895–1903.

[11] X. Tan, Y. Xu, X. Yang, Z. Liu, D. Wu, Effect of partitioning procedure on microstructure and mechanical properties of a hot-rolled directly quenched and partitioned steel, Mat. Sci. Eng. A Struct. 594 (2014) 149–160.

[12] M. Wang, C.C. Tasan, D. Ponge, A. Kostka, D. Raabe, Smaller is less stable: size effects on twinning vs. transformation of reverted austenite in TRIP-maraging steels, Acta Mater 79 (2014) 268–281.

[13] G. Gao, H. Zhang, X. Gui, Z. Tan, B. Bai, Y. Weng, Enhanced strain hardening capacity in a lean alloy steel treated by a "disturbed" bainitic austempering process, Acta Mater 101 (2015) 31–39.

[14] H.L. Yi, P. Chen, Z.Y. Hou, N. Hong, H.L. Cai, Y.B. Xu, D. Wu, G.D. Wang, A novel design: partitioning achieved by quenching and tempering (Q-T & P) in an aluminium-added low-density steel, Scripta Mater 68 (2013) 370–374.

[15] Y. Xu, X. Tan, X. Yang, Z. Hu, F. Peng, D. Wu, G. Wang, Microstructure evolution and mechanical properties of a hot-rolled directly quenched and partitioned steel containing proeutectoid ferrite, Mat. Sci. Eng. A Struct. 607 (2014) 460–475.

[16] X. Tan, Y. Xu, D. Ponge, X. Yang, Z. Hu, F. Peng, X. Ju, D. Wu, D. Raabe, Effect of intercritical deformation on microstructure and mechanical properties of a low-silicon aluminum-added hot-rolled directly quenched and partitioned steel, Mat. Sci. Eng. A Struct. 656 (2016) 200–215.

[17] R. Ding, Z. Dai, M. Huang, Z. Yang, C. Zhang, H. Chen, Effect of pre-existed austenite on austenite reversion and mechanical behavior of an Fe-0.2c-8mn-2Al medium MN steel, Acta Mater 147 (2018) 59–69.

[18] A. Molkeri, F. Pahlevani, I. Emmanuelawati, V. Sahajwalla, Thermal and mechanical stability of retained austenite in high carbon steel: an in-situ investigation, Mater Lett. 163 (2016) 209–213.

[19] H.L. Yi, P. Chen, H.K.D.H. Bhadeshia, Optimizing the morphology and stability of retained austenite in a delta-TRIP steel, Metall Mater Trans. A 45A (2014) 3512–3518.

[20] X. Tan, D. Ponge, W. Lu, Y. Xu, X. Yang, X. Rao, et al., Carbon and strain partitioning in a quenched and partitioned steel containing ferrite, Acta Mater 165 (2019) 561–576.

[21] M. Diehl, P. Shanthraj, P. Eisenlohr, F. Roters, Neighborhood influences on stress and strain partitioning in dual-phase microstructures, Meccanica 51 (2016) 429–441.

[22] C. Song, H. Yu, L. Li, T. Zhou, J. Lu, X. Liu, The stability of retained austenite at different locations during straining of I&Q&P steel, Mat Sci. Eng. A Struct. 670 (2016) 326–334.

[23] S.O. Kruijver, L. Zhao, J. Sietsma, S.E. Offerman, N.H. Van Dijk, E.M. Lauridsen, L. Margulies, S. Grigull, H.F. Poulsen, S. Van der Zwaag, In situ observations on the mechanical stability of austenite in TRIP-steel, J. De Phys. IV 104 (2003) 499–502.

[24] X.C. Xiong, B. Chen, M.X. Huang, J.F. Wang, L. Wang, The effect of morphology on the stability of retained austenite in a quenched and partitioned steel, Scripta Mater 68 (2013) 321–324.

[25] H. Lee, M.C. Jo, S.S. Sohn, A. Zargaran, J.H. Ryu, N.J. Kim, et al., Novel medium-Mn (austenite + martensite) duplex hot-rolled steel achieving 1.6GPa strength with 20% ductility by MN-segregation-induced TRIP mechanism, Acta Mater 147 (2018) 247–260.

[26] Y.F. Shen, L.N. Qiu, X. Sun, L. Zuo, P.K. Liaw, D. Raabe, Effects of retained austenite volume fraction, morphology, and carbon content on strength and ductility of nanostructured TRIP-assisted steels, Mat Sci. Eng. A Struct. 636 (2015) 551–564.

[27] C.C. Tasan, J.P.M. Hoefnagels, M. Diehl, D. Yan, F. Roters, D. Raabe, Strain localization and damage in dual phase steels investigated by coupled in-situ deformation experiments and crystal plasticity simulations, Int. J. Plastic. 63 (2014) 198–210.

[28] C.C. Tasan, M. Diehl, D. Yan, C. Zambaldi, P. Shanthraj, F. Roters, D. Raabe, Integrated experimental-simulation analysis of stress and strain partitioning in multiphase alloys, Acta Mater 81 (2014) 386–400.

[29] J.H. Ryu, D. Kim, H.S. Kim, H.K.D.H. Bhadeshia, D. Suh, Strain partitioning and mechanical stability of retained austenite, Scripta Mater 63 (2010) 297–299.

[30] R. Blonde, E. Jimenez-Melero, L. Zhao, N. Schell, E. Brueck, et al., The mechanical stability of retained austenite in low-alloyed trip steel under shear loading, Mat. Sci. Eng. A Struct. 594 (2014) 125–134.

[31] D. Yan, C.C. Tasan, D. Raabe, High resolution in situ mapping of microstrain and microstructure evolution reveals damage resistance criteria in dual phase steels, Acta Mater 96 (2015) 399–409.

[32] C.C. Tasan, M. Diehl, D. Yan, M. Bechtold, F. Roters, L. Schemmann, C. Zheng, N. Peranio, D. Ponge, M. Koyama, K. Tsuzaki, D. Raabe, An overview of dual-phase steels: advances in microstructure-oriented processing and micromechanically guided design. editor D.R. Clarke (Ed.), An overview of dual-phase steels: advances in microstructure-oriented processing and micromechanically guided design, Ann. Rev. Mater. Res. 45 (2015) 391–431.

[33] N. Fujita, N. Ishikawa, F. Roters, C.C. Tasan, D. Raabe, Experimental–numerical study on strain and stress partitioning in bainitic steels with martensite–austenite constituents, Int J. Plastic. 104 (2018) 39–53.

[34] M.M. Wang, J.C. Hell, C.C. Tasan, Martensite size effects on damage in quenching and partitioning steels, Scripta Mater 138 (2017) 1–5.

[35] A. Dutta, D. Ponge, S. Sandlöbes, D. Raabe, Strain partitioning and strain localization in medium manganese steels measured by in situ microscopic digital image correlation, Materialia 5 (2019) 100252.

[36] A. Kumar, A. Dutta, S.K. Makineni, M. Herbig, R.H. Petrov, J. Sietsma, In-situ observation of strain partitioning and damage development in continuously cooled carbide-free bainitic steels using micro digital image correlation, Mater. Sci. Eng. A 757 (2019) 107–116.

[37] E.J. Seo, L. Cho, J.K. Kim, J. Mola, L. Zhao, B.C. De Cooman, Constituent-specific properties in quenching and partitioning (Q&P) processed steel, Mater. Sci. Eng. A 740-741 (2019) 439–444.

[38] Y. Toji, H. Matsuda, D. Raabe, Effect of si on the acceleration of bainite transformation by preexisting martensite, Acta Mater 116 (2016) 250–262.

[39] Y. Toji, G. Miyamoto, D. Raabe, Carbon partitioning during quenching and partitioning heat treatment accompanied by carbide precipitation, Acta Mater 86 (2015) 137–147.

[40] X. Tan, Y. Xu, X. Yang, Z. Hu, F. Peng, X. Ju, et al., Austenite stabilization and high strength-elongation product of a low silicon aluminum-free hot-rolled directly quenched and dynamically partitioned steel, Mater Charact. 104 (2015) 23–30.

[41] J. Zhang, H. Ding, R.D.K. Misra, Enhanced strain hardening and microstructural characterization in a low carbon quenching and partitioning steel with partial austenization, Mat Sci. Eng. A Struct 636 (2015) 53–59.

[42] A. Kwiatkowski Da Silva, G. Leyson, M. Kuzmina, D. Ponge, M. Herbig, S. Sandlöbes, B. Gault, J. Neugebauer, D. Raabe, Confined chemical and structural states at dislocations in Fe-9wt%mn steels: a correlative TEM-atom probe study combined with multiscale modelling, Acta Mater 124 (2017) 305–315.

[43] M. Gouné, S. Aoued, F. Danoix, G. Geandier, A. Poulon-Quintin, J.C. Hell, M. Soler, S.Y.P. Allain, Alloying-element interactions with austenite/martensite interface during quenching and partitioning of a model Fe-C-Mn-Si alloy, Scripta Mater 162 (2019) 181–184.

[44] L. Yuan, D. Ponge, J. Wittig, P. Choi, J.A. Jiménez, D. Raabe, Nanoscale austenite reversion through partitioning, segregation and kinetic freezing: example of a ductile 2GPa Fe−Cr−C steel, Acta Mater 60 (2012) 2790–2804.

[45] Y. Li, D. Raabe, M. Herbig, P.P. Choi, S. Goto, A. Kostka, et al., Segregation stabilizes nanocrystalline bulk steel with near theoretical strength, Phys. Rev. Lett. 113 (2014) 106104.

[46] X. Tan, Y. Xu, X. Yang, D. Wu, Microstructure-properties relationship in a one-step quenched and partitioned steel, Mat Sci. Eng. A Struct. 589 (2014) 101–111.

[47] W. Lu, M. Herbig, C.H. Liebscher, L. Morsdorf, R.K.W. Marceau, G. Dehm, et al., Formation of eta carbide in ferrous martensite by room temperature aging, Acta Mater 158 (2018) 297–312.

[48] L. Morsdorf, C.C. Tasan, D. Ponge, D. Raabe, 3D structural and atomic-scale analysis of lath martensite: effect of the transformation sequence, Acta Mater 95 (2015) 366–377.

[49] M.J. Yao, P. Dey, J.B. Seol, P. Choi, M. Herbig, R.K.W. Marceau, et al., Combined atom probe tomography and density functional theory investigation of the Al off-stoichiometry of kappa-carbides in an austenitic Fe-Mn-Al-C low density steel, Acta Mater 106 (2016) 229–238.

[50] K. Hono, D. Raabe, S.P. Ringer, D.N. Seidman, Atom probe tomography of metallic nanostructures, Mrs Bull. 41 (2016) 23–29.

[51] M. Calcagnotto, D. Ponge, E. Demir, D. Raabe, Orientation gradients and geometrically necessary dislocations in ultrafine grained dual-phase steels studied by 2D and 3D EBSD, Mater. Sci. Eng. A 527 (2010) 2738–2746.

[52] J. Kadkhodapour, S. Schmauder, D. Raabe, S. Ziaei-Rad, U. Weber, M. Calcagnotto, Experimental and numerical study on geometrically necessary dislocations and non-homogeneous mechanical properties of the ferrite phase in dual phase steels, Acta Mater 59 (2011) 4387–4394.

[53] D. Poddar, C. Ghosh, B. Bhattacharya, V.K. Singh, Development of high ductile ultra high strength structural steel through stabilization of retained austenite and stacking fault, Mater. Sci. Eng. A 762 (2019) 138079.

[54] Y. Yang, Z. Mi, M. Xu, Q. Xiu, J. Li, H. Jiang, Impact of intercritical annealing temperature and strain state on mechanical stability of retained austenite in medium mn steel, Mater. Sci. Eng. A 725 (2018) 389–397.

[55] R. Xiong, H. Peng, H. Si, W. Zhang, Y. Wen, Thermodynamic calculation of stacking fault energy of the fe−mn−si−c high manganese steels, Mater. Sci. Eng. A 598 (2014) 376–386.

[56] S. Curtze, V.T. Kuokkala, Dependence of tensile deformation behavior of TWIP steels on stacking fault energy, temperature and strain rate, Acta Mater 58 (2010) 5129–5141.

[57] A. Saeed-Akbari, J. Imlau, U. Prahl, W. Bleck, Derivation and variation in composition-dependent stacking fault energy maps based on subregular solution model in high-manganese steels, Metallurg. Mater. Trans. A 40 (2009) 3076–3090.

[58] S. Curtze, V.T. Kuokkala, A. Oikari, J. Talonen, H. Hänninen, Thermodynamic modeling of the stacking fault energy of austenitic steels, Acta Mater 59 (2011) 1068–1076.

[59] S. Allain, J.P. Chateau, O. Bouaziz, S. Migot, N. Guelton, Correlations between the calculated stacking fault energy and the plasticity mechanisms in fe−mn−c alloys, Mater. Sci. Eng. A 387 (2004) 158–162.

[60] M.M. Wang, C.C. Tasan, D. Ponge, A.C. Dippel, D. Raabe, Nanolaminate transformation-induced plasticity−twinning-induced plasticity steel with dynamic strain partitioning and enhanced damage resistance, Acta Mater 85 (2015) 216–228.

[61] B. Sun, F. Fazeli, C. Scott, X. Yan, Z. Liu, X. Qin, et al., Critical role of strain partitioning and deformation twinning on cracking phenomenon occurring during cold rolling of two duplex medium manganese steels, Scripta Mater 130 (2017) 49–53.

[62] I. de Diego-Calderon, D. De Knijf, M.A. Monclus, J.M. Molina-Aldareguia, I. Sabirov, C. Foejer, et al., Global and local deformation behavior and mechanical properties of individual phases in a quenched and partitioned steel, Mat. Sci. Eng. A Struct. 630 (2015) 27–35.

[63] H.L. Yi, K.Y. Lee, H.K.D.H. Bhadeshia, Mechanical stabilisation of retained austenite in δ-TRIP steel, Mater. Sci. Eng. A 528 (2011) 5900–5903.

[64] L. Morsdorf, O. Jeannin, D. Barbier, M. Mitsuhara, D. Raabe, C.C. Tasan, Multiple mechanisms of lath martensite plasticity, Acta Mater 121 (2016) 202–214.